MUONITH v1.0 — A Fast Simulation Tool for Multi-directional Muography Observation Design

Authors

Seigo Miyamoto [1] (corresponding author) — miyamoto@eri.u-tokyo.ac.jp

Shogo Nagahara [2]

[1] Earthquake Research Institute, The University of Tokyo, Tokyo, Japan

[2] Graduate School of Science, Nagoya University, Nagoya, Aichi, Japan

---

Preprint statement

This is a **non-peer-reviewed preprint** submitted to EarthArXiv.

At the time of posting, this manuscript has not been submitted to a journal for peer review. Subsequent versions of this manuscript may have different content. If accepted for publication, the final version will be available through the *Peer-reviewed Publication DOI* link on the right-hand side of this webpage.

Please feel free to contact the corresponding author with any comments or questions; feedback is welcome.

Software availability

The MUONITH source code and the accompanying tools are openly available. Version and repository details are given in the *Data and code availability* section of this manuscript.

MUONITH v1.0 — A Fast Simulation Tool for Multi-directional Muography Observation Design

Seigo Miyamoto*[1] and Shogo Nagahara[2]

[1]Earthquake Research Institute, The University of Tokyo, Tokyo, Japan
[2]Nagoya University, Graduate School of Science, Nagoya, Aichi, Japan

Abstract

Multi-directional muography is a non-destructive technique for imaging the three-dimensional density structure of large objects such as volcanoes. Recent developments in detector technology—miniaturization, low-power operation, and weight reduction—are rapidly expanding the range of feasible observation sites, and detector deployment by unmanned aerial vehicles (UAVs) is also being studied; in the near future, the number of observation-resource allocation patterns to be considered is expected to increase explosively. Yet for targets representable as a digital elevation model (DEM), no existing tool estimates—rapidly, quantitatively, and independently of detector type—how accurately the target structure can be resolved for each of these many candidate resource allocations.

We present MUONITH (MUOgraphic Numerical Inversion & Tomography Harness), a high-speed simulation platform that estimates the performance of diverse detector configurations for DEM-based targets. The characteristic outputs of v1.0 are the following two: (i) a resolution metric visualizing single-direction detectability on the depth–anomaly-size plane, and (ii) three-dimensional density reconstruction for multi-directional observations via regularized linear inversion with maximum a posteriori (MAP) estimation. Its speed comes from the default flux model based on a continuous slowing down approximation (CSDA) incorporating the mean radiative losses (bremsstrahlung and pair production), which reduces flux evaluation to a two-dimensional lookup table indexed by density-length and zenith angle, together with a C++20 implementation combining Digital Differential Analyzer ray tracing, OpenMP parallelization, and OpenBLAS-accelerated linear algebra.

The culmination of MUONITH v1.0 is that a three-dimensional reconstruction that previously required tens of hours on dedicated computers can now be performed in minutes on a consumer laptop. It achieves a two-to-three-order-of-magnitude speed-up at one-quarter the memory of the earlier GNU Octave implementation, enabling individual researchers without dedicated infrastructure to evaluate observation designs. The tool is also useful for narrowing down a few promising parameter sets before running a high-accuracy Monte Carlo simulator.

1 Introduction

1.1 Significance of Muography and Multi-Directional Observations

Muography is a measurement technique that non-destructively visualizes the internal density distribution of large structures by employing the high penetrating power of secondary cosmic-ray muons produced in the atmosphere. This approach has evolved substantially since the late 2000s[1–6]. Its

*Corresponding author: miyamoto@eri.u-tokyo.ac.jp

applications have been rapidly expanding from volcanology to archaeological sites, large industrial facilities, and nuclear reactors, and several cross-disciplinary review articles have summarized this progress[7–9]. The multi-directional observations addressed in this paper represent the next paradigm common to all these applications—namely, the transition from one- to three-directional projection imaging toward full three-dimensional density tomography. Single-direction measurements provide only the line-integrated density (density-length) along the muon trajectory and lack spatial resolution along the path. Consequently, they cannot independently determine the depth or precise location of the detected density anomalies.

The principle by which multi-directional muon observations overcome the limitations of single-direction measurements is identical to the relationship between medical X-ray CT and conventional radiography. A single radiographic projection provides only the line-integrated X-ray attenuation along the beam path, causing structures located at different depths to overlap within a single image. As a result, although such images can reveal the presence of anomalous shadows in two dimensions, they cannot determine the depth, size, or shape of the underlying structures. In contrast, CT reconstructs three-dimensional structures by solving the inverse problem of multi-directional projections based on the same attenuation physics, thus reconstructing the superposed components as distinct volumetric objects. Multi-directional muography follows the same framework: it reduces the reconstruction of three-dimensional density to an inverse problem in which voxel densities are estimated from line-integrated density measurements obtained along multiple viewing directions. This approach enables the spatial separation of distinct structures that could produce identical density-length values, allowing their positions, scales, shapes, and orientations to be independently quantified. By enabling this capability, the evaluation of the target object advances from the ambiguous statement that "some anomaly exists somewhere along this direction" to a quantitative description of "how much density contrast exists, at what depth and orientation, and with what three-dimensional spatial extent." This increased specificity provides a foundation for concrete decision-making in applications ranging from volcanic hazard assessment and evacuation planning to archaeological investigation and preservation, as well as nuclear-reactor decommissioning.

Multi-directional muography, however, operates under three constraints that X-ray CT does not face. First, the probe is the natural cosmic-ray muon flux, whose intensity cannot be increased at will; the available statistics are fixed by the exposure and the detector acceptance. Second, detectors must be placed on natural terrain, so the dense and uniform angular coverage of a CT gantry is unattainable. Transport and deployment by UAVs is a realistic future prospect (discussed below), but even then the placement remains strongly constrained by the surrounding environment. Third, observation resources—the number of detectors available and the time each of them can be left in the field—are limited. These constraints make it essential to determine, before deployment, what a given observation configuration can and cannot resolve. The observation-design problem addressed in this paper is to quantitatively determine, prior to measurement, the viewing directions, number of detectors, and observation duration required to reconstruct the target structure with the desired three-dimensional spatial resolution using multi-directional muography.

In volcanic imaging, 1–2-direction muography has successfully achieved observations that were previously difficult for conventional geophysical methods, such as confirming the conduit structure at Satsuma-Iōjima[10] and detecting density changes associated with hydrothermal fluid migration at La Soufrière[11]. However, extending muography to multiple viewing directions had long been limited due to constraints on detector placement ([12]; [13]). Nagahara and Miyamoto (2018) [14] conducted a simulation study for volcanic targets to examine the applicability conditions of the analytical inverse-projection method—filtered back projection—commonly used in X-ray CT. They identified the conditions under which three-dimensional density reconstruction becomes feasible when a sufficient number of projection images are combined.

A representative example of the current state of multi-directional muography achieved in real observations is the multi-directional imaging conducted at the Ōmuroyama volcano in the Izu region of Shizuoka Prefecture (580 m a.s.l., basal diameter 1 km, relative height 280 m, a scoria cone formed 4 ka) [15, 16]. Nuclear emulsion detectors optimized for multi-directional observations were deployed at 11 sites, and linear inverse analysis was applied to the projection images from the remaining 10 directions after excluding one site due to poor data quality. This enabled the direct three-dimensional visualization of the central welded conduit corresponding to the main feeder system, as well as three radial dikes: (i) an E–W-trending dike feeding the small lava flow on the western flank, (ii) an SSE–NNW-trending dike associated with the small crater on the southern slope, and (iii) a north-trending dike. An interactive three-dimensional model of this reconstruction is publicly available [17]. These results provide non-destructive constraints on internal volcanic structures that cannot be obtained from surface outcrop observations alone, forming a basis for volcanic hazard assessment, evacuation planning, and dynamical interpretations of magma supply systems and eruption histories.

The applications of muography extend beyond volcanology and are increasingly expanding into the non-destructive inspection of diverse large-scale structures. In archaeology, muography has enabled the discovery of a large void and the measurement of corridor geometries in the Khufu pyramid [18, 19], and three-dimensional reconstruction has been demonstrated by combining multi-view images of the underground cavities beneath Mt. Echia in Naples [20, 21]. In industrial facilities, muography has been applied to measure refractory thickness and reconstruct three-dimensional density structures inside operating blast furnaces [22–25]. In nuclear-reactor decommissioning, muographic imaging has been used to obtain transmission images of fuel debris in the damaged reactors at Fukushima Daiichi [26, 27], and multi-view three-dimensional reconstruction has been reported for the graphite reactor at Marcoule in France [28, 29]. Across these fields, many applications are currently in a developmental stage transitioning from single- or few-direction transmission imaging toward multi-directional observations enabling full three-dimensional reconstruction.

All of these studies are case-specific applications in which observation designs were individually constructed for particular targets and detector configurations, and the analyses were performed using tools developed separately for each project. As such, they do not rely on a systematic evaluation framework that is independent of the detector type. To address this gap, the aim of this paper is to provide a fast simulation platform that enables quantitative assessment of observation-design validity prior to measurement, regardless of the detector type, for any target representable as a DEM.

1.2 Increased Deployment Flexibility Enabled by Improvements in Detector Performance

One of the long-standing bottlenecks in the practical application of muography has been hardware constraints on where detectors can be deployed. Conventional muographic observations have primarily relied on plastic-scintillator detectors [30–32] and multi-wire gas detectors or resistive-plate chambers [33, 34]. Each of these systems has different requirements in terms of weight, power consumption, and environmental robustness, which tended to restrict deployments to locations where large equipment could be transported, electrical power secured, and regular maintenance performed. Although attempts to reconstruct three-dimensional density distributions began in the 2010s, only two or three detector sites could typically be installed, which was insufficient to achieve spatial resolutions meaningful for volcanological interpretation.

In recent years, technological advances have continued to relax deployment constraints for muon detectors, including lightweight and highly mobile compact scintillation arrays and gas detectors, and power-free, high-resolution nuclear emulsion detectors [15, 35, 36]. Extending this trend of miniaturization and power reduction leads to the next stage: if detector weight, power consumption, and environmental robustness satisfy certain conditions, transporting and deploying detectors using unmanned aerial vehicles (UAVs) becomes a realistic option. Indeed, in volcanic observations, UAV-based measurements have already been demonstrated, such as gas-sensor surveys within crater plumes [37] and helicopter-based aerial deployment of seismic and infrasound sensors [38].

For example, when volcanic activity intensifies, access within a radius of several kilometers from the crater may be prohibited. Placing a detector far from the target volcano yields insufficient signal because the subtended solid angle becomes small. If UAV-based transport and installation of detectors becomes practical, detectors could be deployed close to a volcano even during periods of temporarily elevated activity.

This development represents not only a quantitative increase in the number of feasible observation points, but also a qualitative shift in which deployability itself becomes an independent design parameter in observation planning. By combining detector performance and specifications (weight, power, size, and angular acceptance) with UAV transport capabilities, the potential deployment candidates emerge as a multidimensional parameter space, shifting the focus from "selecting from a small number of sites where access and detector installation are feasible" to "optimizing detector placement based on scientific objectives."

1.3 Issues surrounding observation-design software

While hardware capabilities are rapidly expanding the flexibility of detector deployment, the software infrastructure that supports observation design has not kept pace, particularly in terms of computational speed. In multi-directional observations, the combinations of deployment locations, detector orientations, and observation durations form a high-dimensional parameter space—especially when UAV-based transport is considered—leading to a substantial increase in the number of candidate configurations that must be evaluated. To assess numerous deployment patterns for a single observation plan within a practical time frame, each trial must return quantitative evaluation results within a short computation time. Moreover, for observation design to become widely practical, it is desirable that such evaluations be executable locally by individual researchers without relying on dedicated large-scale computing environments.

However, no existing tool was designed for exhaustive observation-design evaluation, so there is currently no systematic means to exploit the potential of multi-directional observations at the design stage. The characteristics of the individual Monte Carlo-based and Python-based tools that leave this gap are examined in the following subsection.

1.4 Comparison with prior work on simulation tools

Existing muography-related simulation and analysis tools can be broadly categorized into Monte Carlo-based frameworks—such as GEANT4 [39] (with muography applications in, e.g., [40]), PUMAS [41], PROPOSAL [42], and MUTE [43, 44]—and lighter Python-based script tools, including SMAUG [45] and MUYSC [46]. Monte Carlo tools provide high-fidelity descriptions of particle-transport physics but incur substantial computational cost per run, which makes it impractical to evaluate candidate observation patterns one after another.

Among existing tools, SMAUG and MUYSC are most closely related to the objectives of the present study. SMAUG is a Python implementation supporting probabilistic inversion using Markov chain Monte Carlo, designed as an educational and research-oriented tool with strong readability and documentation. MUYSC provides an end-to-end Python pipeline—from simplified ray tracing and flux estimation using semi-empirical Gaisser/Tang models to algebraic reconstruction—offering a full-stack workflow for muographic analysis. However, neither tool is optimized to evaluate a single multi-directional observation configuration fast enough that many candidate configurations can be compared before deployment.

MUONITH, developed in this study, is designed to fill this common gap. It occupies a third position distinct from both Monte Carlo-based and script-based approaches. The positioning of these simulation tools relative to MUONITH is illustrated in Figure 1. The intended role of MUONITH is not to serve as a standalone final-analysis tool, but to evaluate each candidate observation design within minutes, so that a researcher can compare candidates and examine only the promising ones in detail using Monte Carlo tools. Automatic screening over large configuration spaces is the goal toward which MUONITH is being developed; in v1.0 the comparison across candidates is still driven by the researcher. This staged workflow allows multi-directional observation design to be performed systematically and efficiently.

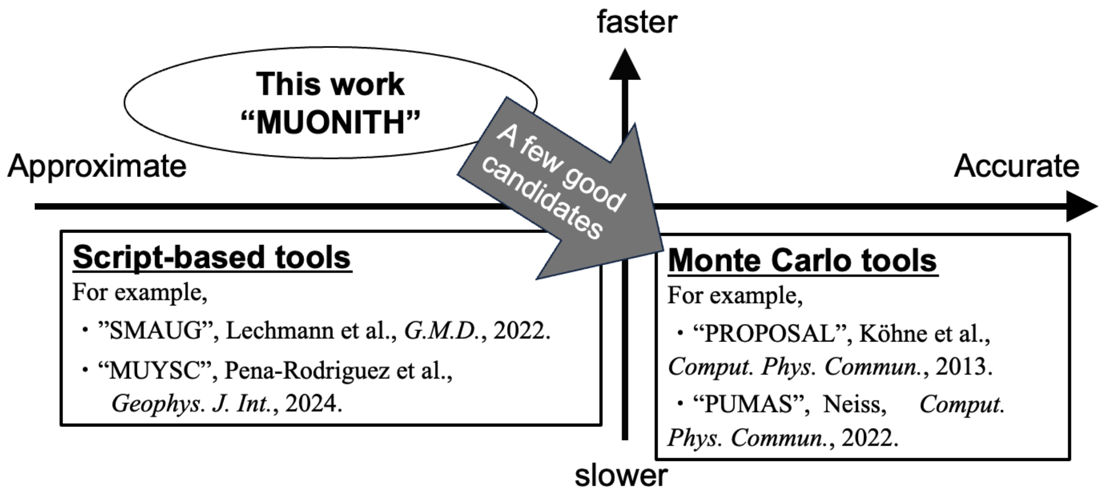

Figure 1: Positioning of MUONITH in the design space of simulation tools for muography. The horizontal axis represents the physical accuracy of signal/noise prediction (left: Approximate, right: Accurate), and the vertical axis represents the evaluation speed for observation patterns (top: faster, bottom: slower)

1.5 Objectives of the Present Study

The central claim of this study can be summarized in a single sentence: MUONITH is a simulation framework that is not tied to any particular detector technology, designed to rapidly and quantitatively evaluate the performance of muography observation configurations—treating both human-accessible deployment sites and potential UAV-transportable sites equivalently—prior to actual measurements.

Three-dimensional density reconstruction is one of MUONITH's important capabilities, but the essential strength of the framework lies in its ability to quickly and quantitatively estimate, for a wide range of observation designs, what results can be obtained from each potential detector placement. Owing to its computational speed, individual observation designs can be evaluated on the order of minutes even on standard consumer-grade laptop environments, without relying on dedicated high-performance computing systems (see "Computational Performance" for quantitative benchmarks).

2 Method

2.1 Concept

MUONITH is built on two core design principles. First, rather than prioritizing the strict reproduction of physical processes through Monte Carlo methods, the framework focuses on rapidly and quantitatively evaluating the feasibility of diverse observation designs, emphasizing broad and fast exploration of the design space over physical exactness. Specifically, a ground-level muon-flux model [47, 48] is combined with a deterministic energy-attenuation table based on the continuous-slowing-down approximation (CSDA) to pre-compute a table of penetrating-muon flux, which is then referenced during the calculation.

Second, MUONITH adopts a geometric model that assumes arbitrary detector placement and orientation on a digital elevation model (DEM), abstracting detector instances as combinations of detector specifications (panel geometry, tilt, distance, and angular segmentation). This enables systematic exploration of potential observation points at the design stage without being limited to locations where detectors can physically be installed. The numerical computation backbone that implements these principles consists of C++20, DDA ray tracing [49], beam-level parallelization using OpenMP, LAPACK linear-algebra libraries based on OpenBLAS or Apple Accelerate, the Eigen sparse-matrix library, and JSON5-based structured configuration files. In addition, multi-platform build environments are provided through Nix (primarily for macOS) and Docker (also operable within Windows Subsystem for Linux).

2.2 Forward simulation

MUONITH takes an observation setup together with terrain and density information as input and computes expected muon-arrival maps for each viewing direction. At the beginning of this section, the overall data flow is presented in Figure 2, followed by three subsections—“Input Information,” “Calculation procedure,” and “Output Information”—which describe the inputs, computational methods, and outputs, respectively.

2.2.1 Input Information

The inputs to the simulation are divided into two groups, as shown on the left side of Figure 2.

The first group consists of muon-physics models. In the standard distribution, the ground-level muon-flux spectrum is based on the daemonflux model [48], and the energy-loss model in crustal material uses the continuous-slowing-down approximation (CSDA) of Groom et al. (2001) [50], which includes the mean of radiative losses but not their fluctuations. These models are pre-convolved into a two-dimensional flux table indexed by density length X and zenith angle θ. Users may replace this table with one generated from their own models (details are provided in “Calculation procedure” of the forward simulation).

The second group consists of observation parameters specified in a JSON5 configuration file. These include the terrain (digital elevation model, DEM; in this study, the standard input is the 5 m mesh DEM (DEM5A) provided by the Geospatial Information Authority of Japan [51], with pre-processing described in the public repository documentation), the density model (uniform density, DEM-attached density, or composite structures such as elliptical cylinders, ellipsoids, or checker-board patterns—“synthetic density structures”), and the detector settings, namely the position

(x, y, z), orientation (yaw, pitch, roll), detector size, pixel size, field-of-view segmentation, number of units, and observation duration. The angular segmentation of the field of view is, by default, defined as equal spacing in the tangent-coordinate system, although degree or radian specification is also available. From these inputs, the path-length matrix L_{ij}, whose element is the length over which beam i crosses voxel j, is constructed, and its product with the input density structure ρ_j yields the density length for each line of sight, $X_i = \sum_j L_{ij}\rho_j$. Finally, combining the density length with the penetrating-muon flux model provides the relationship between density length and expected muon flux for each viewing direction.

Both groups of inputs are read through a single entry point, and virtual observations and real-data analysis share the remainder of the pipeline beyond this entry.

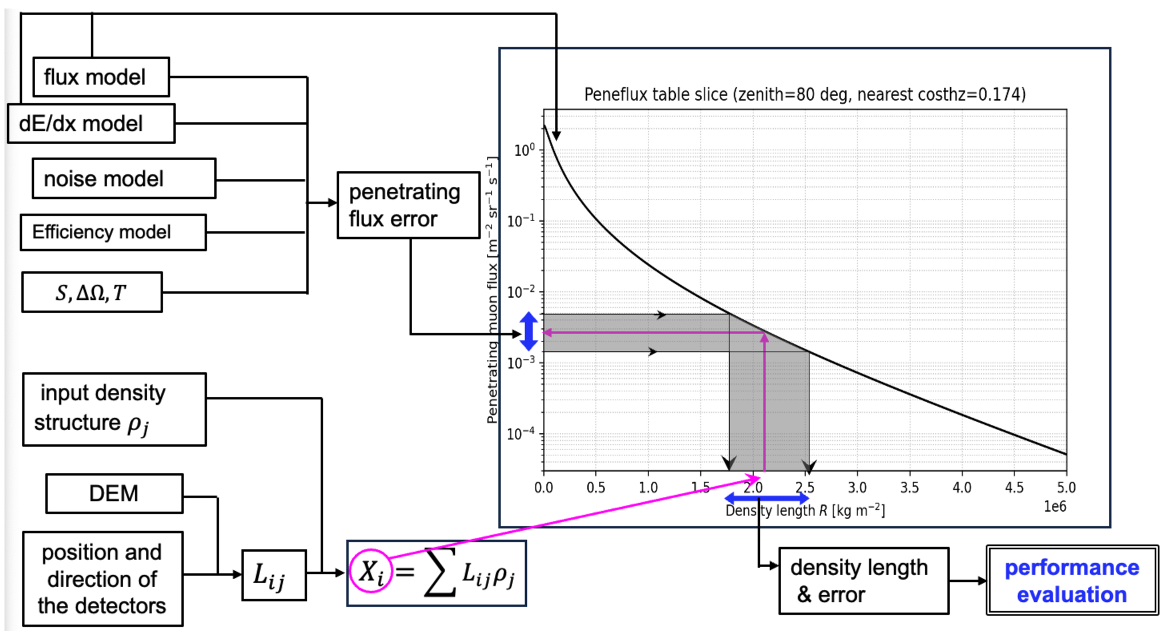

Figure 2: Data flow for performance evaluation in single-direction muography. The blocks on the left represent the inputs. In the upper branch, the flux model and the dE/dx model give the table of penetrating-muon flux, and these together with the noise model, the efficiency model, and the detector acceptance and exposure (S, $\Delta\Omega$, T) give its uncertainty. In the lower branch, the density length along each line of sight is computed from the digital elevation model (DEM) and the position and orientation of the detectors. The plot on the right shows an example of the flux table at a zenith angle of 80°.

2.2.2 Calculation procedure

The procedure for constructing the angular-element set used in the simulation from the detector-placement information is executed collectively as the generation of the detector-panel array. The detector-panel array is the top-level structure that bundles multiple detector panels, and each detector panel contains a two-dimensional array of angular elements defined according to the angular-segmentation specification (an $n_x \times n_y$ bin configuration, field-of-view range, and angular units).

The heavy computations for the angular elements within each detector panel are executed in two parallelized passes. The first pass is the geometric-calculation pass based on DDA ray tracing [49]. For each of the $n_x \times n_y$ angular elements in a detector panel, the path length Λ_i [m] traversed by the line of sight through the terrain-voxel space and the density length X_i [kg/m^2] obtained as the inner product with the density model are computed and assigned to each angular-element instance. Here $\Lambda_i = \sum_j L_{ij}$ is the row sum of the path-length matrix. All lines of sight are assumed to originate from a single representative position of the detector panel. The detector itself is specified as a rectangular box of width, height, and depth, and its size enters the calculation through the effective area S_i, which is evaluated separately for each viewing direction; because of the depth, the open aperture shrinks and S_i decreases as the line of sight becomes more oblique.

The second pass uses the density length X_i obtained in the first pass as input to compute, for each angular element:

(i) the penetrating-muon flux $F(X_i, \theta_i)$ via two-dimensional lookup in the flux table described later;

(ii) the solid angle $\Delta\Omega_i$ determined by the angular-bin geometry;

(iii) the effective area S_i determined by the viewing direction together with the detector orientation, physical dimensions, and number of modules; and

(iv) the expected muon counts

$$N_i = F(X_i, \theta_i) \cdot S_i \cdot \Delta\Omega_i \cdot T_i, \tag{1}$$

where T_i is the observation time, which in the current design is given as a single value common to all angular elements of a detector panel. These values are assigned to each angular-element instance.

The ray-tracing computation and the penetrating-flux lookup are executed sequentially for each detector panel, and the two-dimensional loop over the $(n_x \times n_y)$ angular elements is parallelized using OpenMP. Because the computations for individual angular elements are independent, the total computational cost scales approximately linearly with the number of angular bins.

MUONITH adopts the continuous-slowing-down approximation (CSDA), a deterministic energy-loss model, as its muon-energy-loss treatment [50]. Because CSDA follows only the mean energy loss and ignores its stochastic fluctuations, it is physically less accurate than Monte Carlo methods, but far cheaper: for each zenith angle θ, the relationship between the amount of traversed material (density length X [kg/m^2]) and the penetrating-muon flux $F(X, \theta)$ can be pre-tabulated as a two-dimensional table. This reduces step (i) above to a simple table lookup. CSDA is a fundamental assumption directly tied to the design philosophy of MUONITH—high-speed scanning of observation designs—and is therefore fixed throughout this study.

The worked examples in this paper (Ōmuroyama and Mt. Tokachi) use a flux table built from the Honda et al. (2007) [47] model with the Groom energy-loss model, instead of the standard daemonflux-based table described in "Input Information"; for Ōmuroyama this reproduces the conditions of Nagahara et al. (2022) [16].

To distinguish between the internal computational resolution and the resolution used for density estimation, MUONITH adopts the policy of initially taking angular-bin widths that are sufficiently finer than the detector's physical resolution. For large three-dimensional structures such as volcanoes, even a small change in viewing direction in elevation can cause a large variation in the path length Λ_i through the terrain. Under such conditions—where the path length Λ_i and density length X_i vary nonlinearly within the field of view—passing coarse angular bins, matched to the detector's physical resolution, directly to the DDA ray-tracing stage would cause the single line of sight at the bin center to poorly represent the true distribution within the bin, resulting in bin-dependent systematic errors.

To avoid this, MUONITH performs the initial DDA and flux calculations uniformly on finely segmented minimal angular elements, computing Λ_i, X_i, and the expected muon counts N_i independently for each minimal element. The detector's effective resolution and the required minimum statistical counts are then satisfied by grouping these minimal angular elements in a later stage (the automatic merging described below). Because the physical calculations (fine-grained DDA) are separated from the operational resolution (bin merging), multiple operational bin configurations—with different detector resolutions or statistical thresholds—can be evaluated without recomputing the underlying fine-grained DDA results.

After the per-element computations are completed, MUONITH performs adaptive bin merging—either automatic or user-defined—on a per-panel basis to ensure sufficient statistical counts for subsequent resolution evaluation and three-dimensional reconstruction. Merging is necessary because, as the solid angle of a minimal angular element becomes small, its statistics are no longer sufficient to determine the density: lines of sight that skim the edges of the target object have path lengths approaching zero, whereas those traversing thick regions yield exponentially attenuated penetrating-muon fluxes. The automatic mechanism therefore combines, independently for each detector panel, the angular elements whose total signal plus noise falls below a prescribed threshold; implementation details and parameters are given in the documentation of the public repository. In the user-defined mode, each panel instead reads a list of rectangular angular regions from a text file, which is validated to tile the field of view without overlaps or gaps before the merge is applied. Because the observation matrix $\mathbf{A}_N$ used in "Three-dimensional density reconstruction" is linear with respect to bin merging, the matrix for a merged bin is simply the sum of the matrices of the original bins, so numerical accuracy in subsequent stages is not degraded.

2.2.3 Output Information

The computational outputs consist of four categories of quantities. First, a map of the path length Λ_i [m] for each viewing direction, determined by the terrain and line-of-sight geometry. Second, a map of the expected muon counts N_i for each viewing direction (angular bin), expressed as count values that reflect the observation time, effective area, and solid angle. Third, the integrated density length X_i [kg/m^2] and the projected mean density ρ_{proj} [kg/m^3] $= X_i/\Lambda_i$ (where Λ_i [m] is the path length for the same viewing direction); note that these belong to the input data. Fourth, the bin-configuration information—bin centers, widths, and solid angles—before and after merging, which serves as input for subsequent resolution evaluation and three-dimensional reconstruction.

Examples of these outputs are shown in Figure 3, assuming an effective detector area of $S = 0.2\,\mathrm{m}^2$ and an observation duration equivalent to $T = 120$ days. Figure 3 presents representative MUONITH inputs and outputs for a single viewing direction in the Ōmuroyama configuration ("Simulation setup"). The top row shows the input terrain and the true density model; the middle row shows the path length inside the mountain and the expected muon counts (for both fine bins and after automatic merging); and the bottom row shows the projected density (true value, estimated value, and associated error).

2.3 Evaluation of density and spatial resolution in single-direction observation

The inputs consist of the following. First, detector information: the position and angular orientation of a single detector panel, its effective area S, observation time T, and field-of-view segmentation. Second, target information: the terrain (DEM) and the background uniform density ρ_0. Third, anomaly parameters to be evaluated: the anomaly depth D, diameter l, density contrast $\Delta\rho$ relative to ρ_0, significance level α, and the observation-resource amplification factor η. The factor η represents the effect of increasing $S \times T$ by a factor of η under otherwise identical observation conditions, allowing the impact of enhanced resources to be assessed without rerunning the simulation.

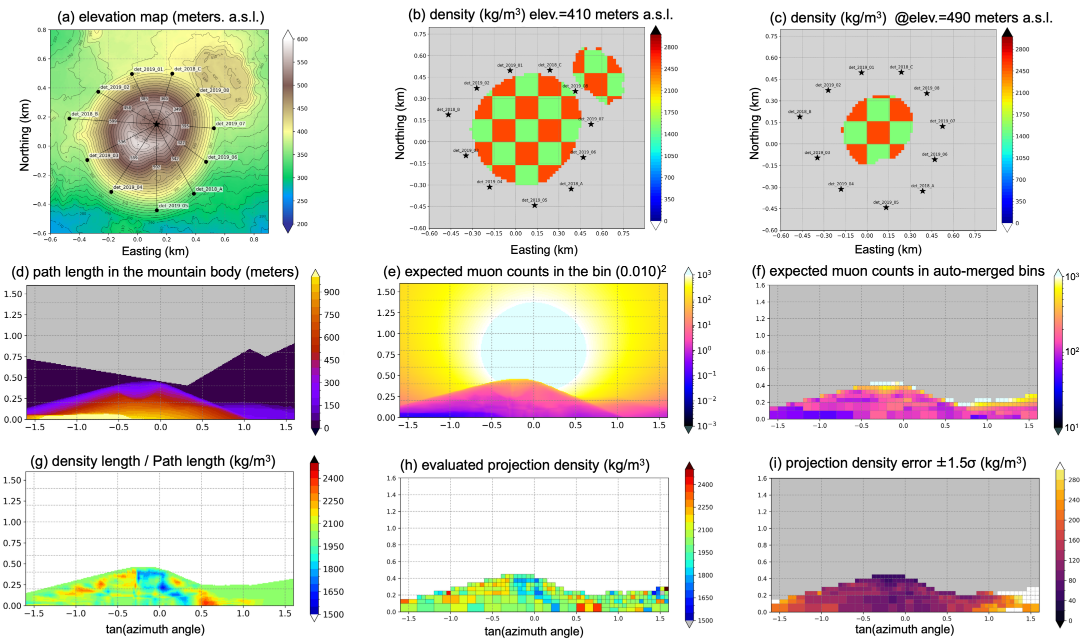

Figure 3: Example of MUONITH input and output for a single viewing direction in the Ōmuroyama configuration (“Simulation setup”). (a) Elevation map (black dots indicate candidate detector locations). (b), (c) Horizontal slices of the true input density model at elevations of 410 and 490 m, respectively. (d) Path length through the mountain. (e) Expected muon counts in fine angular bins of width 0.010 in both tangent-coordinate directions. (f) Expected muon counts after automatic bin merging. (g) True projected mean density. (h) Estimated projected density after automatic bin merging. (i) Projected-density error shown as $\pm 1.5\sigma$. In panels (d)–(i), the horizontal and vertical axes are tan(azimuth angle) and tan(elevation angle), respectively. These panels show the outputs for a single viewing direction at the western observation point (`det_2018_B`) indicated in panel (a).

2.3.1 Calculation method

For each angular element, the path length Λ_i, density length X_i, and penetrating muon flux $F(X_i, \theta_i)$ are computed as in the forward simulation.

In the depth–resolution evaluation, we determine whether an anomaly of diameter l located at depth D, with density contrast $\Delta\rho$, is detectable under a given observation resource $(S \times \Delta\Omega_i \times T)$, where $\Delta\Omega_i$ is the solid-angle element. The decision is based on a two-sample z-test comparing the expected muon counts with and without the anomaly. Let $N(\rho_0 + \Delta\rho)$ be the expected muon count in the presence of the anomaly, and $N(\rho_0)$ the count for the background model. The test statistic is

$$z = \frac{N(\rho_0 + \Delta\rho) - N(\rho_0)}{\sqrt{N(\rho_0 + \Delta\rho) + N(\rho_0)}}. \tag{2}$$

From this, the minimum detectable anomaly size is determined for a given significance level α (e.g., $\alpha = 0.05$).

2.3.2 Output information

The outputs consist of maps of the expected muon counts, projected mean density, and statistical uncertainty for each angular element, as shown in Figure 3, together with either the boundary curve of the detectable region in the depth–anomaly-size plane or a heatmap of $\log_{10}(p)$. In addition, sets of boundary curves corresponding to different values of the observation-resource amplification factor η are produced. Representative output formats are shown in Figure 4 (see “Single-direction resolution evaluation” for discussion of application examples).

In the performance evaluation for single-direction observations, a density anomaly of representative size l is placed at depth D inside a uniform-density body with density ρ_0, where the anomaly density is $\rho = \rho_0 + \Delta\rho$. Detectability is then quantified for a detector characterized by its effective area S, solid angle $\Delta\Omega_i$, and observation time T.

Figure 4(b) includes several geometric annotations: α denotes the exclusion region where the anomaly cube would protrude above the surface (the effect becomes stronger for larger anomalies and steeper slopes); β indicates the elevation level of the detector; γ marks the crater elevation (1728 m a.s.l. in this example); δ represents the geometric boundary preventing the anomaly cube from lying below the detector elevation; ε provides a reference scale corresponding to the anomaly size.

This framework provides a foundation for translating the allocation of observation resources—previously guided largely by intuition and empirical rules—into a visual and quantitative decision-making process.

2.4 Three-dimensional density reconstruction

Three-dimensional density reconstruction is provided as a standard implementation in MUONITH, formulated as a linear inverse problem in which the density of each voxel is inferred from the density-length integrals along multiple viewing directions. The mathematical framework in this section follows Nagahara et al. (2022) (see Appendix C); the linearized derivation of the observation matrix $\mathbf{A}_N$, the posterior distribution under a Gaussian prior in Bayesian inversion, the notation definitions (Table 3), and numerical constraints relevant to implementation are summarized therein.

Briefly, the density-length vector $\mathbf{X}$ is expressed as a linear combination of the voxel-density vector $\boldsymbol{\rho}$ through the path-length matrix $\mathbf{L}$. The observation matrix $\mathbf{A}_N$, obtained by linearizing

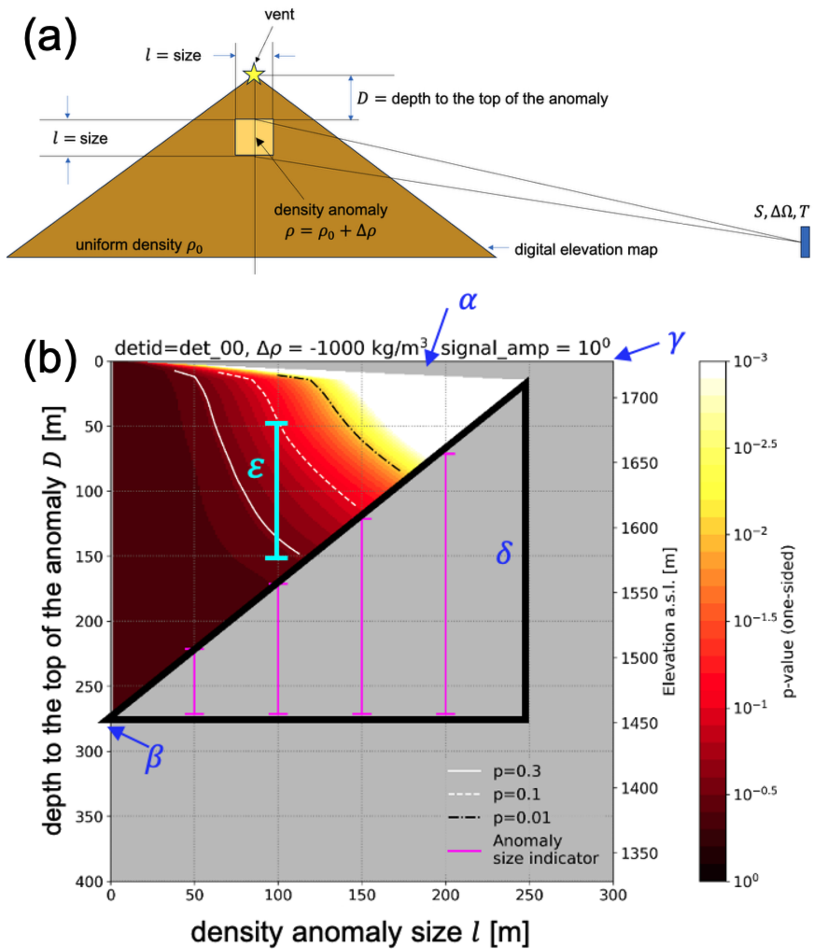

Figure 4: Schematic illustration and representative output formats for detection-limit evaluation (depth vs. spatial resolution) using single-direction observations. (a) Geometry of the evaluation. (b) Detection-limit map (example: `detid=det_00`, $\Delta\rho = -1000\,\mathrm{kg/m^3}$, `signal_amp` $= 10^0$, effective area $S = 0.2\,\mathrm{m}^2$, observation time $T = 120$ days). The color scale indicates the one-sided p-value corresponding to the statistical difference between the expected muon counts without the anomaly, $N(\rho_0)$, and with the anomaly, $N(\rho_0 + \Delta\rho)$. The magenta vertical bar indicates a reference anomaly size, and the black triangular envelope marks the geometrically evaluable region (excluding cases where the anomaly protrudes above the ground surface due to terrain constraints).

the expected muon counts around the prior density length, is linear with respect to the bin merging described in "Calculation procedure" of the forward simulation.

2.4.1 Voxel Merging and Treatment of Terrain Boundaries

Voxel merging lowers the reconstruction resolution in order to keep the problem size tractable; the dominant reason is memory, because the prior covariance matrix is stored in dense form and its cost grows as the square of the number of voxels (see "Limitations and Applications"). Merging aggregates a specified number of subdivisions (e.g., 4 per axis) into a single large voxel, but only when all voxels within the $n_x \times n_y \times n_z$ merge unit are fully contained within the terrain; the merged density is then the average of the original densities. Voxels that straddle the terrain boundary are left at their original fine-scale subdivision.

As a result, the domain is divided into two regions: the voxels that are the targets of the three-dimensional reconstruction, and a shell-like region that follows the terrain and consists of what remains once those reconstruction-target voxels are removed. Only the former are included as unknowns in the linear inversion, whereas the latter are assigned known or assumed densities and contribute to the path-length integrals but are excluded from the degrees of freedom of the reconstruction.

In addition, the user may specify a reconstruction sub-volume in the form of an axis-aligned bounding box or an elliptical cylinder. Restricting the inversion to physically meaningful portions of a large domain improves computational efficiency and stabilizes the solution.

2.5 Use of AI-assisted tools

Parts of the MUONITH source code and of the manuscript draft were prepared with the assistance of large language models. The authors reviewed, tested and edited all such output, and take full responsibility for the content of the software and of this paper.

3 Results

3.1 Single-direction resolution evaluation

As a demonstration, we applied it to the fumarole system of the Furiko-zawa crater group on Mt. Tokachi, Hokkaido (crater 62-2; WGS84: 43°25′23″ N, 142°40′31″ E). Using detector `det_00` (effective area $S = 0.2\,\mathrm{m}^2$, observation equivalent to $T = 120$ days), background density $\rho_0 = 2500\,\mathrm{kg/m}^3$, density contrasts $\Delta\rho \in \{-500, -1000\}\,\mathrm{kg/m}^3$, and significance levels $\alpha \in \{0.3, 0.1, 0.01\}$, we plotted the relationship between depth below the 62-2 crater surface and spatial resolution (anomaly size) (Figure 5).

The resulting detection-limit maps (output format shown in Figure 4; application to Mt. Tokachi shown in Figure 5) allow the dependence of detectability on density contrast $\Delta\rho$, anomaly size, and depth to be read quantitatively. Comparing Figures 5(b) and 5(c), the case with the larger absolute density contrast, $\Delta\rho = -1000\,\mathrm{kg/m}^3$ (panel c), exhibits a broader region of significant detectability, extending to smaller and deeper anomalies than the $-500\,\mathrm{kg/m}^3$ case (panel b). The scaling behavior (diminishing returns) associated with varying the observation-resource amplification factor η is discussed in "Scaling and diminishing-returns effect of the observation-resource amplification factor η," where it is used as a basis for considering whether additional resources should extend the observation time in an existing direction or support observation from an additional direction.

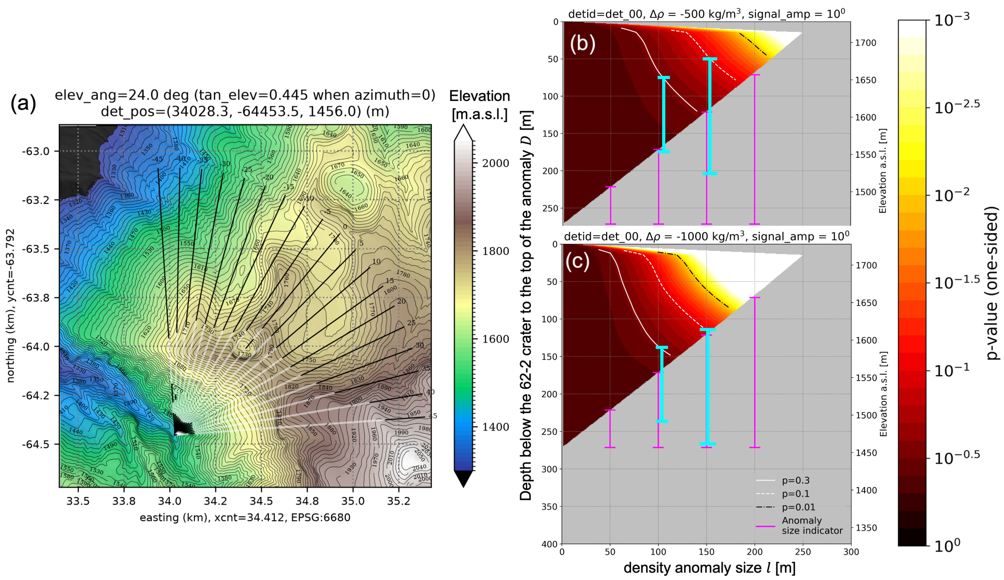

Figure 5: Application example of single-direction muography for the Furiko-zawa fumarole system (crater 62-2) on Mt. Tokachi, Hokkaido. (a) Elevation map and viewing geometry (elevation angle $24.0°$, $\tan(\text{elevation}) = 0.445$). The black segment indicates the muon path in air (outside the mountain), and the white one indicates inside the mountain. (b), (c) Detection-limit maps. The left vertical axis shows depth from the 62-2 crater surface to the top of the anomaly [m]; the right vertical axis shows elevation [m a.s.l.]. Colors represent one-sided p-values. Magenta and cyan vertical bars indicate reference anomaly sizes. (b) Density contrast $\Delta\rho = -500\,\mathrm{kg/m^3}$ (representative of porosity 33% and water saturation $S_w = 1.0$). (c) Density contrast $\Delta\rho = -1000\,\mathrm{kg/m^3}$ (representative of porosity 40% and $S_w = 0.0$).

3.2 Evaluation of three-dimensional density reconstruction

3.2.1 Simulation setup

The benchmark configuration follows the same terrain and detector-placement conditions as the muography observations of Ōmuroyama, Shizuoka, Japan (WGS84: 34°54′14″ N, 139°05′44″ E) reported in Nagahara et al. (2022). The simulation parameters are summarized in Table 1. Using this configuration, MUONITH was executed in forward mode to produce, for each detector panel, maps of expected muon counts, projected density, and the bin configurations before and after merging (see Figure 3 in "Output Information" of the forward simulation for representative examples).

Table 1: Simulation setup for the Ōmuroyama benchmark. Note that the effective area and the observation time differ from those of Nagahara et al. [16].

Item	Setting
Terrain data	Geospatial Information Authority of Japan 5 m mesh DEM (DEM5A) [51], covering approximately $2000 \times 2000\,\mathrm{m}^2$.
Voxel resolution	$20 \times 20 \times 20\,\mathrm{m}^3$ after merging; $z = 200$–$600\,\mathrm{m}$, with 5 m pitch merged by a factor of 4 in the vertical direction.
Detector layout	11 directions following Nagahara et al.[16]; effective area $0.2\,\mathrm{m}^2$ for each detector, 120 observation days, and angular-element size $(0.010)^2 \tan^2$.
Input density	Three-dimensional checkerboard with 200 m interval, background density $2000\,\mathrm{kg/m}^3$ and alternating $\pm\Delta\rho = 500\,\mathrm{kg/m}^3$.
Observation condition	Detector efficiency variation and physical noise from low-momentum particles [4] were not included in the baseline.
Flux model	Honda et al. (2007) [47].
Energy-loss model	Continuous-slowing-down approximation (CSDA) of Groom et al. (2001) [50].

3.2.2 Reconstruction results

Figure 6 shows the results of applying MUONITH's multi-directional linear inversion (Equation (18) of Nagahara et al. 2022; see "Mathematical formulation of three-dimensional density reconstruction") to the "Simulation setup." In the central region, the input checkerboard pattern is qualitatively well reproduced, demonstrating high fidelity in areas where multiple viewing directions intersect densely. Self-evaluation of reconstruction-density errors—statistical error, leave-one-out error, and mixed error—computed solely from the observation data and viewing geometry without reference to the true model is presented in "Estimation of reconstructed-density errors and application to real-data analysis."

In addition, when the reconstruction-parameter set—density uncertainty σ_ρ, spatial correlation length l_c, and prior density—is declared as an array in the JSON5 configuration file, MUONITH automatically performs sequential inversions over the Cartesian product of these parameters in a single binary execution, and the outputs for each parameter combination are saved in separate subdirectories.

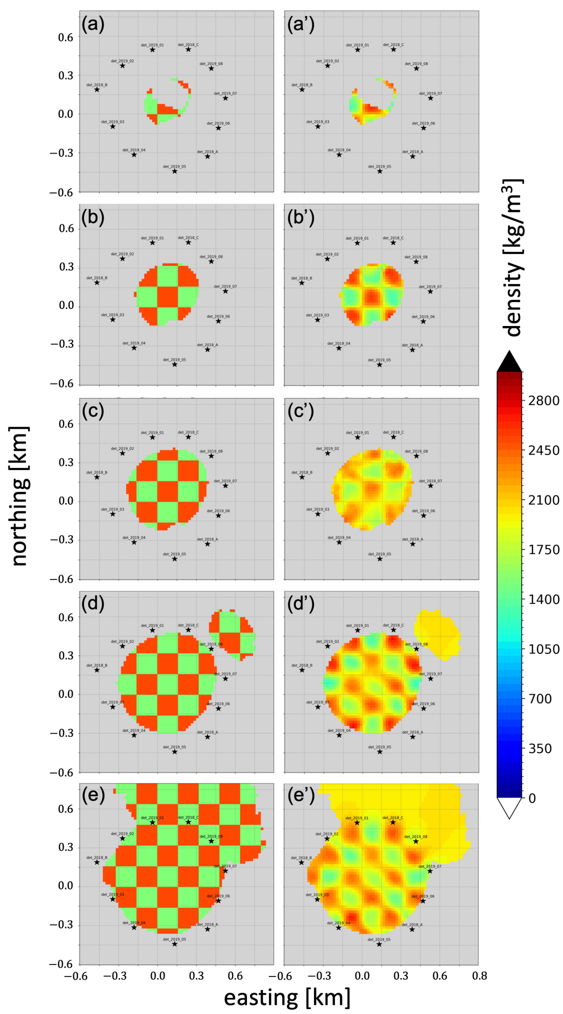

Figure 6: Evaluation of the three-dimensional density reconstruction for Ōmuroyama ($\rho_0 = 2000\,\mathrm{kg/m^3}$, $\pm\Delta\rho = 500\,\mathrm{kg/m^3}$, voxel size 20 m). The 5×2 layout shows horizontal slices of the input checkerboard density in the left column (a)–(e) and the corresponding reconstructed density slices at the same elevations in the right column (a′)–(e′). From top to bottom, the rows correspond to elevations of 530, 490, 450, 410, and 370 m. The horizontal and vertical axes are easting and northing, respectively, both in km. Triangular markers indicate the positions of the 11 detectors, and all panels share the density color scale at right in $\mathrm{kg/m^3}$.

3.2.3 Computational Performance

Table 2 presents a comparison between the earlier implementation by Nagahara et al. (2022)—a GNU Octave–based script—and MUONITH, using measured execution time and memory usage for the same reconstruction problem (“Simulation setup”). Although the two implementations could not be executed on identical hardware and the comparison is therefore not strictly controlled, the reconstruction target, terrain data, and observation conditions are matched.

The primary factors contributing to this performance are:

(i) the C++20 implementation combined with algorithmic optimization via DDA ray tracing;

(ii) large-scale linear algebra enabled by sparse path-length matrices together with Eigen and OpenBLAS/LAPACK; and

(iii) beam-level parallelization using OpenMP.

The CPU utilization reaches 1501 %, corresponding to a parallel efficiency of approximately 54 % relative to the target 28 threads. Remaining bottlenecks include I/O and serial components of the bin-merging process.

Furthermore, the same reconstruction problem was executed on a 2022 consumer-grade business laptop (Intel Core i5-1155G7, 4 cores / 8 threads, 16 GB RAM, WSL Ubuntu 24.04); the runtime and peak memory are listed in Table 2. Although this is not a controlled hardware comparison, it confirms portability.

In addition, running the same reconstruction on an Apple Silicon laptop (MacBook Pro; Apple M4 Pro, 12 cores, 48 GB RAM, macOS 15.7.5) with the linear-algebra backend switched to Apple Accelerate completed in 31.1 seconds (wall-clock; bottom row of Table 2). Regarding memory, the physical memory the process actually allocated—the peak memory footprint—was about 4.1 GB, below the Linux Max RSS (6.4 GB).

From these results, MUONITH demonstrates that (i) single-direction observations can quantitatively evaluate resolution metrics for targets on the scale of Mt. Tokachi, (ii) multi-directional three-dimensional density reconstruction for Ōmuroyama-scale problems ($\sim 10^4$ voxels $\times \sim 10^6$ beams) can be completed within minutes; and (iii) neither a dedicated workstation nor a cluster is required, since reconstructions complete within minutes even on standard laptop-class computing environments.

4 Discussion

In version 1.0, the current stage of development is such that, although the core computational program has been successfully accelerated, the surrounding components—evaluation functions and iterative control algorithms required for fully automated sweeping of large parameter spaces to find the optimal allocation of observation resources—have not yet been implemented. Based on this level of maturity, the following sections describe the extensibility of the tool and its limitations and applicable scope.

4.1 Extensibility of the Tool

MUONITH exports the observation matrix $\mathbf{A}_N$, the observed and prior muon-count vectors $\mathbf{N}_{\mathrm{obs}}$ and $\mathbf{N}_0$, the prior and reconstructed density vectors $\boldsymbol{\rho}_0$ and $\boldsymbol{\rho}'$, voxel coordinates, and row/column mappings as binary datasets, accompanied by text-based JSON manifests describing their layout, units, and reconstruction settings. Selected observation matrices, detector maps, and cross-sectional data can also be exported as ASCII text. Users can therefore test their own reconstruction algorithms in external analysis environments (Python, MATLAB, Octave, R, etc.) without being

Table 2: Computational performance comparison for the Ōmuroyama three-dimensional checkerboard reconstruction using observations from 11 directions.

Method	Implementation and hardware	Runtime	Peak memory
Nagahara et al. [16]	GNU Octave, single-threaded Linux run	about 20 h	about 20–30 GB
MUONITH, server machine	C++20 + OpenMP + OpenBLAS/LAPACK; AMD Ryzen 9 5950X, 28 threads used	47.8 sec wall clock; 645.5 sec user; 72.4 sec system	6.5 GB Max RSS
MUONITH, laptop	Same code; Intel Core i5-1155G7, 4 cores / 8 threads, WSL Ubuntu 24.04	221.8 sec wall clock; 528.9 sec user; 138.4 sec system	about 6.3 GB Max RSS
MUONITH, laptop (macOS)	C++20 + OpenMP + Apple Accelerate/LAPACK; Apple M4 Pro (8P+4E / 12 cores, 9 threads used), macOS 15.7.5, 48 GB RAM	31.1 sec wall clock; 66.3 sec user; 11.6 sec system	about 4.1 GB peak memory footprint

constrained to MUONITH's built-in MAP estimator. Furthermore, because intermediate results (path-length matrix, observation matrix, prior information) can be saved in binary form, iterative reconstructions that modify only the inversion conditions (sweeps over σ_ρ, l_c, and prior density) require re-executing only the inversion module, thereby reducing the computational cost of parameter tuning.

In correlation modeling for three-dimensional density reconstruction, the design of the prior covariance $\mathbf{C}_\rho$ has a substantial impact on the reconstruction results. MUONITH implements not only the default isotropic exponential correlation model but also a separable anisotropic model that allows independent specification of horizontal and vertical correlation lengths. This enables physically motivated priors—for example, assigning a longer horizontal correlation length than vertical for layered sedimentary structures—to be incorporated directly into the reconstruction.

4.2 Limitations and Applications

From the standpoint of physical modeling and numerical methodology, the first limitation is that CSDA does not account for energy-loss fluctuations or multiple scattering, which can introduce systematic errors in density estimation or in special energy regimes; users who need a more precise estimate are therefore advised to first produce several rough candidate designs with MUONITH and then pass the promising detector placements to a Monte Carlo-based tool. In addition, note that applying the reconstruction-parameter set used in the demonstration of "Evaluation of three-dimensional density reconstruction" (Section 3.2) directly to smaller structures can excessively smooth steep density gradients or discontinuous structures (e.g., Figure 6). Regarding memory usage, because the covariance matrix is stored in dense form, large-scale problems exceeding roughly 50,000 voxels encounter an $O(n_v^2)$ memory bottleneck of about 10 GB in single precision; at present, voxel merging or specifying reconstruction sub-volumes are the practical workarounds. The current observation-error model adopts a simplified diagonal $\mathbf{C}_N$ based on a Poisson approximation. Detector efficiency and its uncertainty can be supplied within MUONITH as a per-angular-bin table listing the central efficiency together with its lower and upper bounds, whereas a non-diagonal

$\mathbf{C}_N$ incorporating the remaining detector systematics (geometry uncertainties, background-model errors) is expected to be implemented externally by researchers using the exported intermediate data (the observation matrix, the observed and prior muon counts, the row/column ordering, and the solved equation, written together with a manifest file).

There are also limitations in representing target geometries. At present, reliable evaluation is essentially restricted to DEMs augmented with basic synthetic three-dimensional structures (DEM + α). To directly handle structures that cannot be represented by a DEM, future development must include support for ingesting CAD-derived geometric models.

5 Conclusion

To support observation planning for multi-directional muography, we are developing MUONITH, a high-speed simulation tool that supports observation-design evaluation for any target representable as a DEM—independent of detector type and deployment conditions—within a single environment spanning pre-observation design through post-observation data analysis. As reported in Section 3 (Table 2), MUONITH reconstructs the Ōmuroyama benchmark in minutes on both workstation and laptop hardware—about two to three orders of magnitude faster than the earlier GNU Octave implementation of Nagahara et al. (2022), at roughly one-quarter the peak memory.

The principal contributions of MUONITH are as follows. It provides a generalized detector model in which arbitrary detector positions, orientations, fields of view, solid-angle binning, and exposure times can be defined in JSON5. For single-direction observations, MUONITH quantifies resolution metrics by evaluating detection boundaries on the depth–anomaly-size plane (see Section 2), enabling practical assessment under realistic JSON5 configurations for actual volcanoes such as Mt. Tokachi. For multi-directional observations, a regularized linear inversion is provided as a standard implementation (see Appendix C). Through binary input/output of intermediate results, MUONITH allows users to sweep inversion conditions while keeping detector geometry fixed, and to integrate user-defined reconstruction algorithms. By unifying virtual design and real-data analysis within a single pipeline, MUONITH enables seamless workflows from pre-observation design evaluation to post-observation reconstruction.

MUONITH is intended to complement detailed Monte Carlo-based tools and script-based frameworks such as SMAUG and MUYSC, forming a foundation for integrated workflows that span observation design, sensitivity evaluation, and real-data analysis. In version 1.0, MUONITH has reached the stage where single-direction resolution evaluation and multi-directional three-dimensional density reconstruction—based on the generalized detector model—can be completed within minutes even on consumer-grade laptops. Future work includes fully automated sweeping of large observation-configuration parameter spaces using evaluation functions and iterative control, optimization of reconstruction for arbitrary three-dimensional geometries, and development of calibration and background-correction pipelines for ingesting real observational data.

Acknowledgements

This work was supported by JSPS KAKENHI Grant Numbers JP25H01293, JP21H05086 and JP19H01988.

Author contributions

S.N. established the basis of the density reconstruction method. Building on that work, S.M. implemented and tested it in MUONITH. S.M. prepared the outline of the manuscript and S.N. wrote the text; S.M. revised it. All authors reviewed and approved the final manuscript.

Competing interests

The authors declare no competing interests.

Data and code availability

MUONITH is openly available at `https://github.com/seigomiyamoto/muonith`; the results reported in this paper were produced with version 1.0.0 (tag `v1.0.0`). The two companion tools used for terrain preparation and viewing-path inspection are available at `https://github.com/seigomiyamoto/muonith-gsi-dem` and `https://github.com/seigomiyamoto/muonith-path-view`. The terrain data used in this study are the 5 m mesh digital elevation model (DEM5A) of the Fundamental Geospatial Data published by the Geospatial Information Authority of Japan [51]; muonith-gsi-dem converts the distributed archives into the form MUONITH reads. The Ōmuroyama observation data are those of Nagahara et al. (2022) [16, 17].

Appendix

A Synthetic density structures

Via JSON5, arbitrary artificial density structures can be generated in the three-dimensional voxel space. The available structures are checkerboards (two-dimensional / three-dimensional), ellipsoids, elliptical cylinders, and so on. Each structure is given a relative density $\Delta\rho$ with respect to the background density, allowing density contrasts to be evaluated. Multiple structures can also be superimposed to imitate complex internal structures, which is used to verify the reconstruction accuracy of inverse-analysis algorithms before actual observation. See the docs of the public repository for the list of structure types that can be generated and how to configure them.

B Scaling and diminishing-returns effect of the observation-resource amplification factor η

The detection limit depends on the observation resource $S\times T$ and on the solid angle $\Delta\Omega$ through the field-of-view division. The solid angle can be gained by shortening the distance to the observation target, but when the target is a volcano there is an accompanying trade-off: closing the distance too much makes it impossible to see through the deeper parts of the edifice. The observation-resource amplification factor η is defined in "Calculation method" of the evaluation of density and spatial resolution in single-direction observation. Owing to the $\sqrt{N}$ property of Poisson statistics, increasing $S \times T$ shifts the detection boundary toward smaller anomalies and greater depths, but the improvement from $\times 10 \to \times 100$ is smaller than that from $\times 1 \to \times 10$, and a diminishing-returns effect is clearly observed. This diminishing-returns assessment provides a basis for deciding whether additional observation resources should be allocated to extending the observation time in an existing direction or to observing from an additional direction. Figure 7 shows the scaling of the detection boundary and the diminishing-returns effect when the observation-resource amplification factor η is varied as $\times 1, \times 10, \times 100$.

Table 3: Notation list for 3D density reconstruction.

Symbol	Dimension	Meaning	Category
$\mathbf{L}$	$n_d \times n_v$	Path-length matrix. L_{ij} is the geometric path length [m] over which beam i traverses voxel j (computed by DDA ray tracing)	input
$\boldsymbol{\rho}_0$	$n_v \times 1$	Prior density [kg/m^3]	input
σ_ρ	scalar	Density uncertainty [kg/m^3]	input
l_c	scalar	Spatial correlation length [m] (horizontal and vertical independently specifiable)	input
$\mathbf{N}_{\mathrm{obs}}$	$n_d \times 1$	Observed muon counts	input
$\mathbf{C}_N$	$n_d \times n_d$	Error covariance of the muon counts (diagonal; the variance of the detector-efficiency uncertainty may be added to the Poisson term)	input
$\left.\dfrac{dN_i}{dX_i}\right\|_{X_{0,i}}$	$n_d \times 1$	Differential sensitivity of the muon transmission spectrum at angular element i; the value evaluated at the prior density length $X_{0,i}$, precomputed from the table of the penetrating muon flux F	input
X_i	scalar	Density length at angular element i [kg/m^2]	intermediate
$\mathbf{A}_N$	$n_d \times n_v$	Observation matrix. $A_{N,ij} = \partial N_i/\partial \rho_j \approx L_{ij} \cdot dN_i/dX_i\|_{X_{0,i}}$	intermediate
$\mathbf{C}_\rho$	$n_v \times n_v$	Prior density covariance (smoothness constraint)	intermediate
$\mathbf{N}_0$	$n_d \times 1$	Expected muon counts based on the prior model	intermediate
$\boldsymbol{\rho}'$	$n_v \times 1$	Reconstructed density (posterior mean)	output
$\mathbf{C}_{\rho'}$	$n_v \times n_v$	Posterior density covariance	output

C Mathematical formulation of three-dimensional density reconstruction

This appendix provides the mathematical details outlined in "Three-dimensional density reconstruction," following Nagahara et al. [16].

The relation between the voxel density vector $\boldsymbol{\rho}$ (of dimension n_v) on the three-dimensional voxel space and the density length X_i at each angular element i is given by

$$X_i = \sum_j L_{ij}\, \rho_j \tag{3}$$

where L_{ij} is the geometric path length in m over which beam i traverses voxel j, computed by DDA ray tracing (Appendix E). The expected muon count in each beam is expressed as a nonlinear

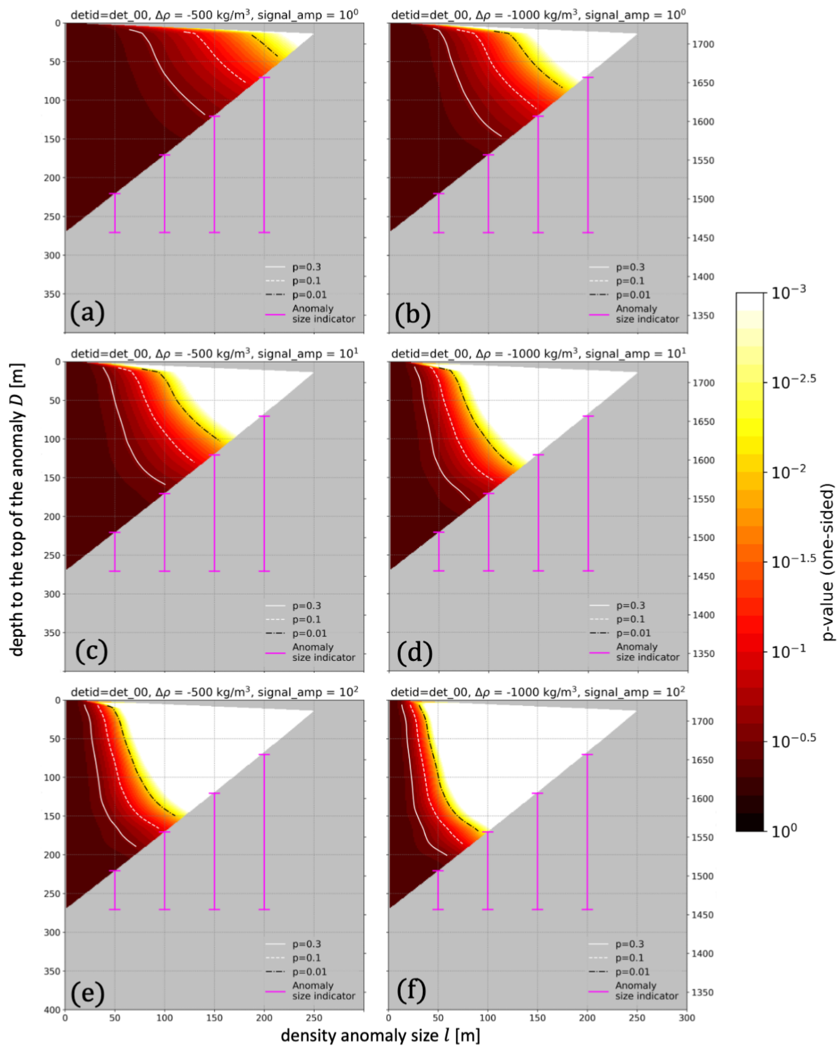

Figure 7: Scaling and diminishing-returns effect of the observation-resource amplification factor η (detector `det_00`; the Furiko-zawa fumarole group / 62-2 crater of Mt. Tokachi, Hokkaido; the same target and basic settings as Figure 5). In a 3-row × 2-column layout, the rows correspond to the observation-resource amplification factor $\texttt{signal\_amp} = \eta = 10^0\,(\times 1),\ 10^1\,(\times 10),\ 10^2\,(\times 100)$ (from top to bottom), and the columns to the density contrasts $\Delta\rho = -500\,\mathrm{kg/m^3}$ (left; (a)(c)(e)) and $\Delta\rho = -1000\,\mathrm{kg/m^3}$ (right; (b)(d)(f)). In each panel the horizontal axis is the size of the density anomaly $l\,[\mathrm{m}]$, the left vertical axis is the depth $D\,[\mathrm{m}]$ to the top of the anomaly, and the right vertical axis is the elevation [m a.s.l.]. The color is the one-sided p-value; the contours are $p = 0.3$ (white solid), 0.1 (white dashed), and 0.01 (black dash-dotted); the magenta vertical bar is a guide for the anomaly size; the gray area indicates the region geometrically excluded from the evaluation. Raising η expands the detection boundary (the p contours) toward smaller anomalies and greater depths, but the width of the expansion from $\times 10 \to \times 100$ is smaller than that from $\times 1 \to \times 10$, from which the diminishing-returns effect can be read.

function of the density length,

$$N_i = g_i(X_i) \tag{4}$$

where g_i is the function obtained by multiplying the CSDA flux-table lookup at the i-th angular element by the effective area, the solid angle, and the observation time. Linearizing around the prior density length $X_{0,i} = \sum_j L_{ij}\,\rho_{0,j}$, the muon-count sensitivity matrix $\mathbf{A}_N$ (the observation matrix) can be written as

$$A_{N,ij} = \frac{\partial N_i}{\partial \rho_j} \approx L_{ij} \cdot \left.\frac{dN_i}{dX_i}\right|_{X_{0,i}} \tag{5}$$

(Eq. (18) of Nagahara et al. [16]). Here dN_i/dX_i is the differential sensitivity obtained from the muon transmission spectrum and is evaluated from differences of the CSDA table. Because this form of $\mathbf{A}_N$ is linear with respect to bin consolidation, it has the numerical advantage that each row of the observation matrix can be treated as a simple sum even under adaptive bin merging (see "Calculation procedure" of the forward simulation).

Following the framework of Bayesian inverse analysis with a Gaussian prior [52], in the formulation of the previous study [5] that applied it to the three-dimensional density-structure reconstruction of the Showa-Shinzan lava dome integrating muon transmission observations and surface gravity-anomaly observations, the posterior density $\boldsymbol{\rho}'$ is obtained as

$$\mathbf{C}_{\rho'} = \left(\mathbf{A}_N^\top \mathbf{C}_N^{-1} \mathbf{A}_N + \mathbf{C}_\rho^{-1}\right)^{-1} \tag{6}$$

$$\delta\boldsymbol{\rho} = \mathbf{C}_{\rho'}\,\mathbf{A}_N^\top \mathbf{C}_N^{-1}(\mathbf{N}_{\mathrm{obs}} - \mathbf{N}_0) \tag{7}$$

$$\boldsymbol{\rho}' = \boldsymbol{\rho}_0 + \delta\boldsymbol{\rho} \tag{8}$$

See Table 3 for the symbol definitions and the input/output classification of each quantity.

Even when the uncertainty of the detector efficiency is included in the evaluation, MUONITH treats $\mathbf{C}_N$ as a diagonal matrix. This is not a claim that correlated efficiency errors do not exist; rather, it is because the efficiency table consumed by MUONITH gives only the median and the upper and lower ends of the efficiency of each angular element, and does not specify the correlation coefficients between angular bins or between detectors, nor a common calibration source. In this paper we assume that the efficiency errors are fully correlated within each merged angular bin and uncorrelated between different merged bins. Under this assumption, the efficiency uncertainty that co-varies within the same merged bin can be folded into the diagonal component as the variance term of that bin. On the other hand, a common calibration error spanning an entire detector or multiple detectors is a quantity that should properly be represented as off-diagonal components, but it is not treated in the fast evaluation model of this paper. This is because the main use of MUONITH is the comparison of observation layouts and relative contrasts, and the rigorous evaluation of systematic errors in absolute density belongs to a stage that should be carried out separately with an explicitly stated correlation model.

Let the angular elements contained in a merged angular bin g be $k \in g$, the median efficiency in the efficiency table be ε_k, and the half-width between the upper and lower ends be

$$\delta\varepsilon_k = \frac{1}{2}\left(\varepsilon_{\mathrm{upp},k} - \varepsilon_{\mathrm{low},k}\right). \tag{9}$$

Let b_k be the reference count before the efficiency is applied.

Writing the element count at the median efficiency as $N_k = \varepsilon_k b_k$, the relative uncertainty as $s_k = \delta\varepsilon_k/\varepsilon_k$, and the merged count as $N_g = \sum_{k\in g} N_k$, in the relative notation of the merged bin used in the discussion,

$$s_g = \frac{\sum_{k\in g} s_k N_k}{N_g}, \qquad (s_g N_g)^2 \tag{10}$$

is the variance term of the efficiency uncertainty. Here $s_k N_k = \delta\varepsilon_k b_k$, so the component that co-varies within the same group by default is written, in the absolute notation used in the implementation, as

$$\sigma^2_{\varepsilon,g} = \left(\sum_{k \in g} \delta\varepsilon_k b_k \right)^2 . \tag{11}$$

When treated as components independent per angular element,

$$\sigma^2_{\varepsilon,g} = \sum_{k \in g} (\delta\varepsilon_k b_k)^2 \tag{12}$$

is used. The diagonal component of $\mathbf{C}_N$ is therefore the Poisson variance N_g plus the variance of the efficiency uncertainty,

$$(\mathbf{C}_N)_{gg} = N_g + \sigma^2_{\varepsilon,g}. \tag{13}$$

This term does not replace the statistical error; it is a term added in quadrature as the uncertainty of the observed counts.

In addition to the default exponential (isotropic) prior covariance, MUONITH implements a separable anisotropic correlation in which the horizontal and vertical correlation lengths are specified independently.

$$C_{\rho,ij} = \sigma^2_\rho \exp\left(-\frac{d_{ij}}{l_c} \right) \tag{14}$$

MUONITH uses matrix representations by Eigen and platform-native LAPACK linear-algebra libraries. The inverse of the posterior covariance $\mathbf{C}_{\rho'}$ is computed by LU decomposition. Both single and double precision can be selected, with single precision as the default (double precision for ill-conditioned problems). As the constraint that the covariance matrix requires $O(n_v^2)$ memory in dense representation, the memory reaches about 10 GB in single precision when the number of voxels exceeds about 50,000, which is set as the safety threshold. When this is exceeded, resolution coarsening or specification of a reconstruction subvolume (see "Voxel Merging and Treatment of Terrain Boundaries") is recommended.

D Estimation of reconstructed-density errors and application to real-data analysis

In real-data analysis of muography the true values of the reconstructed density are not available, so the reconstruction error cannot be measured as the difference from the truth. Furthermore, even if the three-dimensional density used as the input of the forward computation (the truth) is compared directly with the reconstructed three-dimensional density, high-frequency components beyond the three-dimensional spatial resolution of the reconstruction merely appear as errors, and this does not serve as a metric expressing the reliability of the reconstruction. The error must therefore be self-evaluated from the observation data and the observation conditions alone, and MUONITH implements this self-evaluation in the same framework as Nagahara et al. [16].

MUONITH estimates the density error of the three-dimensional density reconstruction (Appendix C; see "Evaluation of three-dimensional density reconstruction") without reference to the truth. For each voxel j, the mixed error $\delta\rho_{\mathrm{total},j}$ is the root sum of squares of the prior error, the statistical error, and the leave-one-out error,

$$\delta\rho_{\mathrm{total},j} = \sqrt{\delta\rho^2_{\mathrm{prior},j} + \delta\rho^2_{\mathrm{post},j} + \delta\rho^2_{\mathrm{LOO},j}} \tag{15}$$

$$\delta\rho_{\mathrm{prior},j} = \frac{1}{2}\left|\rho_{\mathrm{upp},j} - \rho_{\mathrm{low},j}\right|, \qquad \delta\rho_{\mathrm{post},j} = \sqrt{(\mathbf{C}_{\rho'})_{jj}}, \qquad \delta\rho_{\mathrm{LOO},j} = \max_k \left|\rho_j'^{(k)} - \rho_j'\right| \tag{16}$$

Here $\rho_{\mathrm{upp},j}$ and $\rho_{\mathrm{low},j}$ are the upper and lower ends of the prior density model; $\mathbf{C}_{\rho'}$ is the posterior covariance of Eq. (6), so that $\delta\rho_{\mathrm{post}}$ is the statistical error originating from the noise covariance $\mathbf{C}_N$; and $\boldsymbol{\rho}'^{(k)}$ is the reconstruction with detector k omitted (11 runs here, one per detector), which is compared with the reconstruction $\boldsymbol{\rho}'$ using all detectors, so that $\delta\rho_{\mathrm{LOO}}$ expresses the dependence of each voxel on the viewing-field arrangement (the robustness of the observation geometry). All three terms are obtained from the observation data and the observation geometry alone, and can be applied as they are to real-data analysis where the truth is not available. These three density-error maps are shown in Figure 8 for the observation data generated by the forward computation of MUONITH (Ōmuroyama, 11 directions, the same settings as Figure 6).

E Intermediate data storage/output and extensibility to user-defined reconstruction

The storage and partial recomputation of intermediate results, and the output of intermediate data for external tools, are both mechanisms for reusing the intermediate results of MUONITH. The former aims at reducing computational cost, the latter at extending the analysis independently of the internal reconstruction logic.

E.1 Binary storage of intermediate results and partial-recomputation strategy

The intermediate results of each computation stage (the path-length computation results, the observation matrix, the prior information, and so on) can be individually saved to and reloaded from binary files. In addition, a coarse checkpoint mechanism is provided that stops the computation at an intermediate stage and restarts from the saved intermediate results. This makes the following operations possible.

- Iterative comparison of reconstructions in which only the inverse-analysis conditions (regularization strength or prior density) are changed.
- Switching the density contrast or the noise conditions while keeping the DEM and the detector placement unchanged.
- Recomputing only some of the stages.

Depending on the parameter to be changed, the stage from which re-execution must start is organized as in Table 4.

See the docs of the public repository for the storage targets of the intermediate results and for how to operate the checkpoints.

E.2 Intermediate data output for external tools

MUONITH exports the observation matrix $\mathbf{A}_N$, the observed and prior muon-count vectors $\mathbf{N}_{\mathrm{obs}}$ and $\mathbf{N}_0$, the prior and reconstructed density vectors $\boldsymbol{\rho}_0$ and $\boldsymbol{\rho}'$, voxel coordinates, and row/column mappings as binary datasets, accompanied by text-based JSON manifests describing their layout, units, and reconstruction settings. Selected observation matrices, detector maps, and cross-sectional data can also be exported as ASCII text.

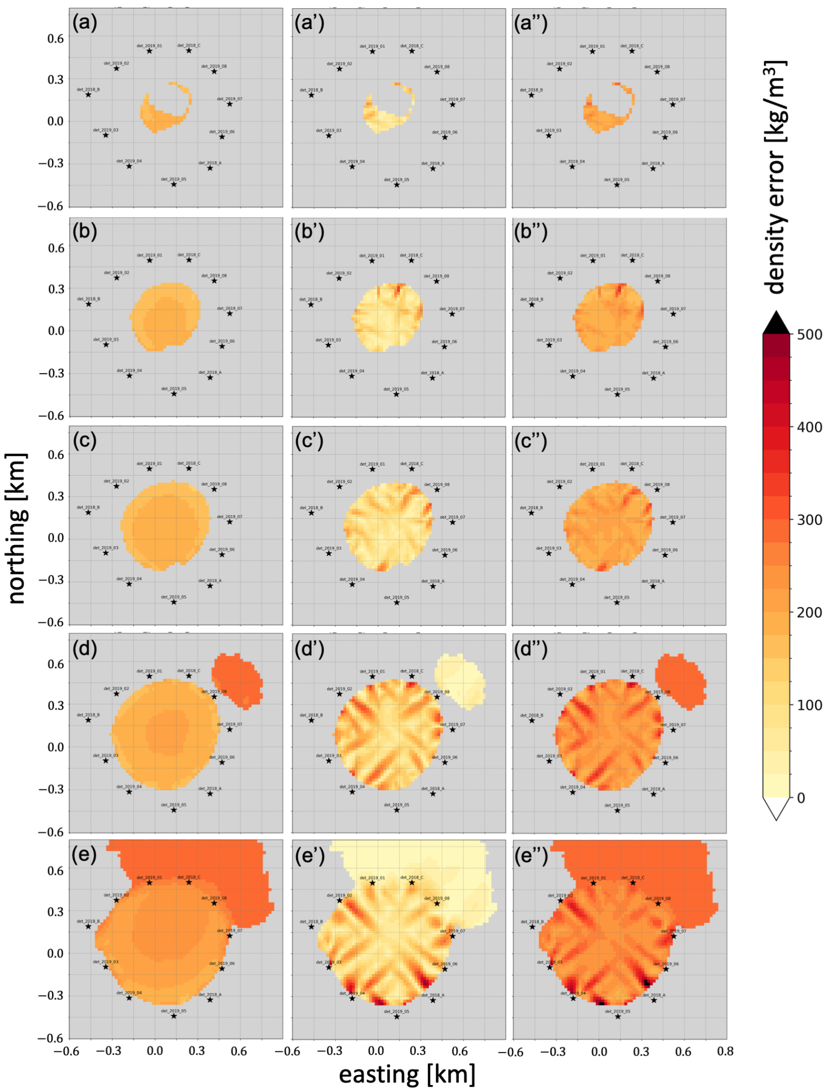

Figure 8: Estimation of the density errors in the Ōmuroyama three-dimensional density reconstruction ($\rho_0 = 2000\,\mathrm{kg/m^3}$, $\pm\Delta\rho = 500\,\mathrm{kg/m^3}$, voxel $20\,\mathrm{m}$, the same settings as Figure 6). In a 5-row $\times$ 3-column layout, the rows correspond to five cross-sections at different elevations, from top to bottom at elevations of $530, 490, 450, 410, 370\,\mathrm{m}$ (descending elevation). The left column (a)–(e) shows the statistical error originating from the noise covariance $\mathbf{C}_N$, the middle column (a′)–(e′) the leave-one-out error obtained by omitting one detector in each run, and the right column (a″)–(e″) the mixed error combining the prior error, the statistical error, and the leave-one-out error in root sum of squares. The horizontal axis is easting and the vertical axis is northing (both in [km]). The group of triangular markers in each panel indicates the 11 detector positions, and the common vertical color bar at the right end is the density error [kg/m^3] (range 0–500). A tendency can be read that the error is small in the central part where the fields of view intersect densely and increases in the peripheral parts where the lines of sight are sparse.

Table 4: Starting stage of re-execution for each changed parameter.

Changed parameter	Starting stage of re-execution
Detector position / attitude	Trace Path Lengths
DEM / grid extent	Build Geometry
Voxel resolution (merge)	Build Geometry
Density uncertainty σ_ρ / horizontal correlation length / vertical correlation length	Invert Density
Uniform prior density	Compute Prior
Flux table	Compute Prior

References

[1] H. K. M. Tanaka, T. Nakano, S. Takahashi, J. Yoshida, M. Takeo, J. Oikawa, T. Ohminato, Y. Aoki, E. Koyama, H. Tsuji, and K. Niwa. High resolution imaging in the inhomogeneous crust with cosmic-ray muon radiography: The density structure below the volcanic crater floor of Mt. Asama, Japan. *Earth and Planetary Science Letters*, 263(1-2):104–113, 2007. ISSN 0012-821X. doi:10.1016/j.epsl.2007.09.001.

[2] N. Lesparre, D. Gibert, J. Marteau, Y. Déclais, D. Carbone, and E. Galichet. Geophysical muon imaging: feasibility and limits. *Geophysical Journal International*, 183(3):1348–1361, 12 2010. ISSN 0956-540X. doi:10.1111/j.1365-246X.2010.04790.x.

[3] D. Carbone, D. Gibert, J. Marteau, M. Diament, L. Zuccarello, and E. Galichet. An experiment of muon radiography at Mt Etna (Italy). *Geophysical Journal International*, 196(2):633–643, 02 2014. ISSN 0956-540X. doi:10.1093/gji/ggt403.

[4] R. Nishiyama, S. Miyamoto, and N. Naganawa. Experimental study of source of background noise in muon radiography using emulsion film detectors. *Geoscientific Instrumentation, Methods and Data Systems*, 3(1):29–39, 2014. doi:10.5194/gi-3-29-2014.

[5] R. Nishiyama, Y. Tanaka, S. Okubo, H. Oshima, H. K. M. Tanaka, and T. Maekawa. Integrated processing of muon radiography and gravity anomaly data toward the realization of high-resolution 3-D density structural analysis of volcanoes: Case study of Showa-Shinzan lava dome, Usu, Japan. *Journal of Geophysical Research: Solid Earth*, 119(1):699–710, 2014. doi:10.1002/2013JB010234.

[6] V. Tioukov, A. Alexandrov, C. Bozza, L. Consiglio, N. D'Ambrosio, G. De Lellis, C. De Sio, F. Giudicepietro, G. Macedonio, S. Miyamoto, R. Nishiyama, M. Orazi, R. Peluso, A. Sheshukov, C. Sirignano, S. M. Stellacci, P. Strolin, and H. K. M. Tanaka. First muography of Stromboli volcano. *Scientific Reports*, 9(1):6695, 2019. ISSN 2045-2322. doi:10.1038/s41598-019-43131-8.

[7] L. Bonechi, R. D'Alessandro, and A. Giammanco. Atmospheric muons as an imaging tool. *Reviews in Physics*, 5:100038, 2020. ISSN 2405-4283. doi:10.1016/j.revip.2020.100038.

[8] G. Bonomi, P. Checchia, M. D'Errico, D. Pagano, and G. Saracino. Applications of cosmic-ray muons. *Progress in Particle and Nuclear Physics*, 112:103768, 2020. ISSN 0146-6410. doi:10.1016/j.ppnp.2020.103768.

[9] H. K. M. Tanaka, C. Bozza, A. Bross, E. Cantoni, O. Catalano, G. Cerretto, A. Giammanco, J. Gluyas, I. Gnesi, M. Holma, T. Kin, I. L. Roche, G. Leone, Z. Liu, D. L. Presti, J. Marteau, J. Matsushima, L. Oláh, N. Polukhina, S. S. V. S. Ramakrishna, M. Sellone, A. H. Shinohara, S. Steigerwald, K. Sumiya, L. Thompson, V. Tioukov, Y. Yokota, and D. Varga. Muography. *Nature Reviews Methods Primers*, 3(1):88, 2023. ISSN 2662-8449. doi:10.1038/s43586-023-00270-7.

[10] H. K. M. Tanaka, T. Uchida, M. Tanaka, H. Shinohara, and H. Taira. Cosmic-ray muon imaging of magma in a conduit: Degassing process of Satsuma-Iwojima Volcano, Japan. *Geophysical Research Letters*, 36(1):L01304, 2009. doi:10.1029/2008GL036451.

[11] K. Jourde, D. Gibert, J. Marteau, J. de Bremond d'Ars, and J.-C. Komorowski. Muon dynamic radiography of density changes induced by hydrothermal activity at the La Soufrière of Guadeloupe volcano. *Scientific Reports*, 6(1):33406, 2016. doi:10.1038/srep33406.

[12] H. K. M. Tanaka, H. Taira, T. Uchida, M. Tanaka, M. Takeo, T. Ohminato, Y. Aoki, R. Nishitama, D. Shoji, and H. Tsuiji. Three-dimensional computational axial tomography scan of a volcano with cosmic ray muon radiography. *Journal of Geophysical Research: Solid Earth*, 115 (B12):B12332, 2010. doi:10.1029/2010JB007677.

[13] M. Rosas-Carbajal, K. Jourde, J. Marteau, S. Deroussi, J.-C. Komorowski, and D. Gibert. Three-dimensional density structure of La Soufrière de Guadeloupe lava dome from simultaneous muon radiographies and gravity data. *Geophysical Research Letters*, 44(13):6743–6751, 2017. doi:10.1002/2017GL074285.

[14] S. Nagahara and S. Miyamoto. Feasibility of three-dimensional density tomography using dozens of muon radiographies and filtered back projection for volcanos. *Geoscientific Instrumentation, Methods and Data Systems*, 7(4):307–316, 2018. doi:10.5194/gi-7-307-2018.

[15] S. Miyamoto, S. Nagahara, K. Morishima, T. Nakano, M. Koyama, and Y. Suzuki. A muographic study of a scoria cone from 11 directions using nuclear emulsion cloud chambers. *Geoscientific Instrumentation, Methods and Data Systems*, 11(1):127–147, 2022. doi:10.5194/gi-11-127-2022.

[16] S. Nagahara, S. Miyamoto, K. Morishima, T. Nakano, M. Koyama, and Y. Suzuki. Three-dimensional density tomography determined from multi-directional muography of the Omuroyama scoria cone, Higashi–Izu monogenetic volcano field, Japan. *Bulletin of Volcanology*, 84(10):94, 2022. doi:10.1007/s00445-022-01596-y.

[17] S. Nagahara, S. Miyamoto, K. Morishima, T. Nakano, M. Koyama, and Y. Suzuki. 3D density imaging by 10-directional muon tomography. Earthquake Research Institute, the University of Tokyo (CHEER), 2022. URL `https://www.eri.u-tokyo.ac.jp/CHEER/data/omuro3ds/`. Interactive three-dimensional density model. Accessed 25 July 2026.

[18] K. Morishima, M. Kuno, A. Nishio, N. Kitagawa, Y. Manabe, M. Moto, F. Takasaki, H. Fujii, K. Satoh, H. Kodama, K. Hayashi, S. Odaka, S. Procureur, D. Attié, S. Bouteille, D. Calvet, C. Filosa, P. Magnier, I. Mandjavidze, M. Riallot, B. Marini, P. Gable, Y. Date, M. Sugiura,

Y. Elshayeb, T. Elnady, M. Ezzy, E. Guerriero, V. Steiger, N. Serikoff, J.-B. Mouret, B. Charlès, H. Helal, and M. Tayoubi. Discovery of a big void in Khufu's Pyramid by observation of cosmic-ray muons. *Nature*, 552(7685):386–390, 2017. doi:10.1038/nature24647.

[19] S. Procureur, K. Morishima, M. Kuno, Y. Manabe, N. Kitagawa, A. Nishio, H. Gomez, D. Attié, A. Sakakibara, K. Hikata, M. Moto, I. Mandjavidze, P. Magnier, M. Lehuraux, T. Benoit, D. Calvet, X. Coppolani, M. Kebbiri, P. Mas, H. Helal, M. Tayoubi, B. Marini, N. Serikoff, H. Anwar, V. Steiger, F. Takasaki, H. Fujii, K. Satoh, H. Kodama, K. Hayashi, P. Gable, E. Guerriero, J.-B. Mouret, T. Elnady, Y. Elshayeb, and M. Elkarmoty. Precise characterization of a corridor-shaped structure in Khufu's Pyramid by observation of cosmic-ray muons. *Nature Communications*, 14(1):1144, 2023. doi:10.1038/s41467-023-36351-0.

[20] L. Cimmino, G. Baccani, P. Noli, L. Amato, F. Ambrosino, L. Bonechi, M. Bongi, V. Ciulli, R. D'Alessandro, M. D'Errico, S. Gonzi, B. Melon, G. Minin, G. Saracino, L. Scognamiglio, P. Strolin, and L. Viliani. 3D muography for the search of hidden cavities. *Scientific Reports*, 9(1):2974, 2019. doi:10.1038/s41598-019-39682-5.

[21] G. Saracino, L. Amato, F. Ambrosino, G. Antonucci, L. Bonechi, L. Cimmino, L. Consiglio, R. D'Alessandro, E. D. Luzio, G. Minin, P. Noli, L. Scognamiglio, P. Strolin, and A. Varriale. Imaging of underground cavities with cosmic-ray muons from observations at Mt. Echia (Naples). *Scientific Reports*, 7(1):1181, 2017. doi:10.1038/s41598-017-01277-3.

[22] K. Nagamine, H. K. M. Tanaka, S. N. Nakamura, K. Ishida, M. Hashimoto, A. Shinotake, M. Naito, and A. Hatanaka. Probing the inner structure of blast furnaces by cosmic-ray muon radiography. *Proceedings of the Japan Academy, Series B*, 81(7):257–260, 2005. doi:10.2183/pjab.81.257.

[23] L. Bonechi, F. Ambrosino, P. Andreetto, G. Bonomi, D. Borselli, S. Bottai, T. Buhles, I. Calliari, P. Checchia, U. Chiarotti, C. Cialdai, R. Ciaranfi, L. Cimmino, V. Ciulli, R. D'Alessandro, M. D'Errico, R. Ferretti, F. Finke, A. Franzen, B. Glaser, S. Gonzi, Y. Liu, A. Lorenzon, V. Masone, O. Nechyporuk, L. Pezzato, B. V. Rangavittal, D. Ressegotti, G. Saracino, J. Sauerwald, O. Starodubtsev, and L. Viliani. BLEMAB European project: muon imaging technique applied to blast furnaces. *Journal of Instrumentation*, 17(04):C04031, 2022. doi:10.1088/1748-0221/17/04/C04031.

[24] D. Borselli, F. Ambrosino, P. Andreetto, L. Bonechi, G. Bonomi, S. Bottai, T. Buhles, I. Calliari, P. Checchia, U. Chiarotti, C. Cialdai, R. Ciaranfi, L. Cimmino, V. Ciulli, R. D'Alessandro, P. G. De Seta Cosentino, E. Faraci, F. Finke, A. Franzen, C. Frosin, C. Gennari, B. Glaser, S. Gonzi, A. Lorenzon, V. Masone, V. Moroli, O. Nechyporuk, A. Paccagnella, L. Pezzato, B. V. Rangavittal, D. Ressegotti, G. Saracino, R. P. Santos Ferreira, J. Sauerwarld, O. Starodubtsev, H. Upadhyay, F. Volzone, and M. Vynnycky. Muon imaging of a blast furnace: The European project BLEMAB. *Journal of Applied Physics*, 138(8):084902, 2025. doi:10.1063/5.0272969.

[25] A. Cohu, A. Chevalier, O. Nechyporuk, A. Franzen, J. Sauerwald, J.-C. Ianigro, and J. Marteau. First 3D reconstruction of a blast furnace using muography. *Journal of Instrumentation*, 18(07):P07004, 2023. doi:10.1088/1748-0221/18/07/P07004.

[26] H. Fujii, K. Hara, K. Hayashi, H. Kakuno, H. Kodama, K. Nagamine, K. Sato, S.-H. Kim, A. Suzuki, T. Sumiyoshi, K. Takahashi, F. Takasaki, S. Tanaka, and S. Yamashita. Investigation of the Unit-1 nuclear reactor of Fukushima Daiichi by cosmic muon radiography. *Progress of Theoretical and Experimental Physics*, 2020(4):043C02, 2020. doi:10.1093/ptep/ptaa027.

[27] H. Fujii, M. Gi, K. Hara, S. Hashimoto, K. Hayashi, H. Kakuno, H. Kodama, M. Mizokami, S. Mizokami, K. Nagamine, K. Sato, S. Sekita, H. Shirai, S.-H. Kim, T. Sumiyoshi, A. Suzuki, Y. Takada, K. Takahashi, Y. Takahashi, F. Takasaki, D. Yamada, and S. Yamashita. Investigation of the status of Unit 2 nuclear reactor of the Fukushima Daiichi by cosmic muon radiography. *Progress of Theoretical and Experimental Physics*, 2021(2):023C01, 2021. doi:10.1093/ptep/ptaa137.

[28] S. Procureur, D. Attié, L. Gallego, H. Gomez, P. Gonzales, B. Lefèvre, M. Lehuraux, B. Lesage, I. Mandjavidze, P. Mas, and D. Pomarède. 3D imaging of a nuclear reactor using muography measurements. *Science Advances*, 9(5):eabq8431, 2023. doi:10.1126/sciadv.abq8431.

[29] B. Lefevre, J. Vogel, H. Gomez, D. Attié, L. Gallego, P. Gonzales, B. Lesage, P. Mas, and D. Pomarède. 3D reconstruction of a nuclear reactor by muon tomography: Structure validation and anomaly detection. *PRX Energy*, 4(1):013002, 2025. doi:10.1103/PRXEnergy.4.013002.

[30] Y. Yamashina, T. Yamashina, H. Taira, and H. K. M. Tanaka. Development of a cost-effective plastic scintillator for cosmic-ray muon radiography of a volcano. *Earth, Planets and Space*, 62(2):173–177, 2010. doi:10.5047/eps.2009.03.003.

[31] N. Lesparre, D. Gibert, J. Marteau, J.-C. Komorowski, F. Nicollin, and O. Coutant. Density muon radiography of La Soufrière of Guadeloupe volcano: comparison with geological, electrical resistivity and gravity data. *Geophysical Journal International*, 190(2):1008–1019, 2012. doi:10.1111/j.1365-246X.2012.05546.x.

[32] J. Marteau, J. de Bremond d'Ars, B. Carlus, A. Chevalier, A. Cohu, T. Descombes, D. Gibert, J.-C. Ianigro, K. Jourde, B. Kergosien, N. Lesparre, J.-L. Montorio, and M. Rosas-Carbajal. Development of scintillator-based muon detectors for muography. In *Muography: Exploring Earth's Subsurface with Elementary Particles*, Geophysical Monograph Series, pages 237–252. Wiley, 2022. doi:10.1002/9781119722748.ch17.

[33] L. Oláh, G. G. Barnaföldi, G. Hamar, H. G. Melegh, G. Surányi, and D. Varga. CCC-based muon telescope for examination of natural caves. *Geoscientific Instrumentation, Methods and Data Systems*, 1(2):229–234, 2012. doi:10.5194/gi-1-229-2012.

[34] C. Cârloganu, V. Niess, S. Béné, E. Busato, P. Dupieux, F. Fehr, P. Gay, D. Miallier, B. Vulpescu, P. Boivin, C. Combaret, P. Labazuy, I. Laktineh, J.-F. Lénat, L. Mirabito, and A. Portal. Towards a muon radiography of the Puy de Dôme. *Geoscientific Instrumentation, Methods and Data Systems*, 2(1):55–60, 2013. doi:10.5194/gi-2-55-2013.

[35] G. Hamar, G. Surányi, D. Varga, G. Nyitrai, L. Oláh, Á. Gera, Sz. J. Balogh, and G. G. Barnaföldi. Underground muography with portable gaseous detectors. *Journal of Physics: Conference Series*, 2374(1):012186, 2022. doi:10.1088/1742-6596/2374/1/012186.

[36] H. Rokujo, K. Sugimura, S. Yamamoto, H. Hayashi, M. Nakamura, Y. Nakamura, T. Nakano, O. Sato, and I. Usuda. Nuclear emulsion film production system for experiments in full-area scanning and analysis era. *Nuclear Instruments and Methods in Physics Research Section A: Accelerators, Spectrometers, Detectors and Associated Equipment*, 1066:169622, 2024. doi:10.1016/j.nima.2024.169622.

[37] K. Wood, E. J. Liu, T. Richardson, R. Clarke, J. Freer, A. Aiuppa, G. Giudice, M. Bitetto, K. Mulina, and I. Itikarai. BVLOS UAS operations in highly-turbulent volcanic plumes. *Frontiers in Robotics and AI*, 7:549716, 2020. doi:10.3389/frobt.2020.549716.

[38] W.-Z. Song, R. Huang, M. Xu, A. Ma, B. Shirazi, and R. LaHusen. Air-dropped sensor network for real-time high-fidelity volcano monitoring. In *Proceedings of the 7th international conference on Mobile systems, applications, and services*, pages 305–318, 2009. doi:10.1145/1555816.1555847.

[39] S. Agostinelli, J. Allison, K. Amako, J. Apostolakis, H. Araujo, P. Arce, M. Asai, D. Axen, S. Banerjee, G. Barrand, F. Behner, L. Bellagamba, J. Boudreau, L. Broglia, A. Brunengo, H. Burkhardt, S. Chauvie, J. Chuma, R. Chytracek, G. Cooperman, G. Cosmo, P. Degtyarenko, A. Dell'Acqua, G. Depaola, D. Dietrich, R. Enami, A. Feliciello, C. Ferguson, H. Fesefeldt, G. Folger, F. Foppiano, A. Forti, S. Garelli, S. Giani, R. Giannitrapani, D. Gibin, J. J. Gómez Cadenas, I. González, G. Gracia Abril, G. Greeniaus, W. Greiner, V. Grichine, A. Grossheim, S. Guatelli, P. Gumplinger, R. Hamatsu, K. Hashimoto, H. Hasui, A. Heikkinen, A. Howard, V. Ivanchenko, A. Johnson, F. W. Jones, J. Kallenbach, N. Kanaya, M. Kawabata, Y. Kawabata, M. Kawaguti, S. Kelner, P. Kent, A. Kimura, T. Kodama, R. Kokoulin, M. Kossov, H. Kurashige, E. Lamanna, T. Lampén, V. Lara, V. Lefebure, F. Lei, M. Liendl, W. Lockman, F. Longo, S. Magni, M. Maire, E. Medernach, K. Minamimoto, P. Mora de Freitas, Y. Morita, K. Murakami, M. Nagamatu, R. Nartallo, P. Nieminen, T. Nishimura, K. Ohtsubo, M. Okamura, S. O'Neale, Y. Oohata, K. Paech, J. Perl, A. Pfeiffer, M. G. Pia, F. Ranjard, A. Rybin, S. Sadilov, E. D. Salvo, G. Santin, T. Sasaki, N. Savvas, Y. Sawada, S. Scherer, S. Sei, V. Sirotenko, D. Smith, N. Starkov, H. Stoecker, J. Sulkimo, M. Takahata, S. Tanaka, E. Tcherniaev, E. Safai Tehrani, M. Tropeano, P. Truscott, H. Uno, L. Urban, P. Urban, M. Verderi, A. Walkden, W. Wander, H. Weber, J. P. Wellisch, T. Wenaus, D. C. Williams, D. Wright, T. Yamada, H. Yoshida, and D. Zschiesche. Geant4—a simulation toolkit. *Nuclear Instruments and Methods in Physics Research Section A: Accelerators, Spectrometers, Detectors and Associated Equipment*, 506(3):250–303, 2003. doi:10.1016/S0168-9002(03)01368-8.

[40] R. Nishiyama, A. Taketa, S. Miyamoto, and K. Kasahara. Monte Carlo simulation for background study of geophysical inspection with cosmic-ray muons. *Geophysical Journal International*, 206(2):1039–1050, 2016. doi:10.1093/gji/ggw191.

[41] V. Niess. The PUMAS library. *Computer Physics Communications*, 279:108438, 2022. doi:10.1016/j.cpc.2022.108438.

[42] J.-H. Köhne, K. Frantzen, M. Schmitz, T. Fuchs, W. Rhode, D. Chirkin, and J. Becker Tjus. PROPOSAL: A tool for propagation of charged leptons. *Computer Physics Communications*, 184(9):2070–2090, 2013. doi:10.1016/j.cpc.2013.04.001.

[43] A. Fedynitch, W. Woodley, and M.-C. Piro. On the accuracy of underground muon intensity calculations. *The Astrophysical Journal*, 928(1):27, 2022. doi:10.3847/1538-4357/ac5027.

[44] W. Woodley, A. Fedynitch, and M.-C. Piro. Cosmic ray muons in laboratories deep underground. *Physical Review D*, 110(6):063006, 2024. doi:10.1103/PhysRevD.110.063006.

[45] A. Lechmann, D. Mair, A. Ariga, T. Ariga, A. Ereditato, R. Nishiyama, C. Pistillo, P. Scampoli, M. Vladymyrov, and F. Schlunegger. SMAUG v1.0 – a user-friendly muon simulator for the imaging of geological objects in 3-D. *Geoscientific Model Development*, 15(6):2441–2473, 2022. doi:10.5194/gmd-15-2441-2022.

[46] J. Peña-Rodríguez, J. Jaimes-Teherán, K. Dlaikan-Castillo, and L. A. Núñez. MUYSC: an end-to-end muography simulation toolbox. *Geophysical Journal International*, 237(1):540–556, 2024. doi:10.1093/gji/ggae064.

[47] M. Honda, T. Kajita, K. Kasahara, S. Midorikawa, and T. Sanuki. Calculation of atmospheric neutrino flux using the interaction model calibrated with atmospheric muon data. *Physical Review D*, 75(4):043006, 2007. doi:10.1103/PhysRevD.75.043006.

[48] J. P. Yañez and A. Fedynitch. Data-driven muon-calibrated neutrino flux. *Physical Review D*, 107(12):123037, 2023. doi:10.1103/PhysRevD.107.123037.

[49] J. Amanatides and A. Woo. A fast voxel traversal algorithm for ray tracing. In *EG 1987-Technical Papers*, pages 3–10. Eurographics Association, 1987. doi:10.2312/egtp.19871000.

[50] D. E. Groom, N. V. Mokhov, and S. I. Striganov. Muon stopping power and range tables 10 Mev–100 Tev. *Atomic Data and Nuclear Data Tables*, 78(2):183–356, 2001. doi:10.1006/adnd.2001.0861.

[51] Geospatial Information Authority of Japan. Fundamental Geospatial Data: Digital Elevation Model, 5 m mesh (DEM5A, airborne laser survey). `https://service.gsi.go.jp/kiban/app/map/?search=dem`, 2026. Accessed 29 July 2026.

[52] A. Tarantola. *Inverse Problem Theory and Methods for Model Parameter Estimation.* SIAM, 2005. doi:10.1137/1.9780898717921.